JOURNAL OF THE AMERICAN HELICOPTER SOCIETY **71**, 032002 (2026)

Loads and Stresses on the Mars Helicopter *Ingenuity* Rotor



Anubhav Datta*
Alfred Gessow Professor

Mrinalgouda Patil[1]
Post-Doctoral Associate

William Staruk[2]
Graduate Research Assistant

Alfred Gessow Rotorcraft Center, Department of Aerospace Engineering
University of Maryland, College Park, MD

The aeroelastic loads, stability, and stresses on the Mars Helicopter *Ingenuity* rotor were predicted during its design with a special-purpose three-dimensional rotor structural dynamic analysis. This paper documents that analysis and the insights gained from it. The thin and cold Martian atmosphere, with density 1% of Earth and speed of sound 30% lower, produced sufficient lift but unusually challenging dynamics even with one third the gravity of Earth. The aeroelastic stability was positive but low—about 10–50 times lower than Earth. The stresses and strains on the 5% thin carbon fiber blades were unsteady, complex, and three dimensional, but within material limits. The key conclusion was that the *Ingenuity* rotor was structurally stable and safe for Martian hover and controlled forward flight, even at the lowest Reynolds number and highest Mach number anticipated on Mars. Fundamental gaps in knowledge and tools remained, which must be addressed for larger, more capable rotorcraft in the future.

Nomenclature

A	rotor disk area πR^2, m^2
a	speed of sound, m/s
C_L	rotor lift $\div\ \rho A(\Omega R)^2$, normal to airflow
C_T	rotor thrust $\div\ \rho A(\Omega R)^2$, along shaft
c	local blade chord, m
$\bar{c}$	mean blade chord $\pi R\sigma/N_b$, m
$\mathbf{D}$	6×6 material stiffness matrix
E	modulus of elasticity, N/m^2 (Pa)
G	shear modulus of elasticity, N/m^2 (Pa)
I_b	blade moment of inertia about root, kg-m^2
I_f	blade feathering inertia about root, kg-m^2
Ma	Mach number
M^2c_n	sectional lift per span $\div\ \frac{1}{2}\,\rho\,a^2\,c$
M^2c_n	sectional chord force per span $\div\ \frac{1}{2}\,\rho\,a^2\,c$
M^2c_n	sectional pitching moment about $0.25c$ per span $\div\ \frac{1}{2}\,\rho\,a^2\,c^2$
M_b	blade mass, kg
M_{TIP}	tip Mach number, $\Omega R \div a$
N_b	number of blades
P	power, W
R	rotor radius, m
Re	Reynolds number
RPM	revolutions per minutes
r_C	vortex core radius, m
r_{C0}	initial vortex core radius, m
T	thrust, N
α_S	shaft tilt into flow, degree or rad
γ	Lock number
ϵ_{IJ} or E_{IJ}	blade strain in I-plane along J-axis
θ_{75}	collective pitch at $0.75\ R$, degree
θ_{1C}, θ_{1S}	lateral and longitudinal pitch, degree
μ	advance ratio, air speed $\times \cos\alpha_S \div \Omega R$
$\mu\epsilon$	micro-strain, $\epsilon \times 10^6$
ν	Poisson's ratio
ν_V	air viscosity, Pa-s
ξ	critical damping ratio
ρ	air density, kg/m^3
σ	rotor solidity
σ_{IJ} or S_{IJ}	blade stress in I-plane along J-axis, MPa
ϕ	wake age, radian
ψ	blade azimuth angle, degree or rad
Ω	rotor rotational speed, rad/s or RPM
ω	frequency, rad/s or Hz

Introduction

Gustave-Louis-Marie de Ponton d'Amécourt's invention for which he coined the term hélicoptère (helicopter) in 1863, from the Greek words helikos (helix) and pteron (wing), was a two-bladed coaxial device (Fig. 1). Models were built by a watchmaker and photographed by the legendary Gaspard-Félix Tournachon, who took the pseudonym Félix Nadar, and whose son Paul Nadar, a professional photographer himself, made a print, which survives in the Bibliothèque Nationale de France. A steam-powered model was built in 1865, which survives in the Models room of the Air and Space Museum in Paris-Le Bourget. A hundred and fifty-eight years later, through a miracle of modern engineering,

---

*Corresponding author; email: datta@umd.edu.

Paper presented at the VFS Transformative Vertical Flight Forum, Santa Clara, February 5–8, 2024. Manuscript received March 2024; accepted January 2026.

[1] Currently Loads & Dynamics Engineer, Joby Aviation.

[2] Currently Rotor Dynamics Engineer, Joby Aviation.

DOI: 10.4050/JAHS.71.032002

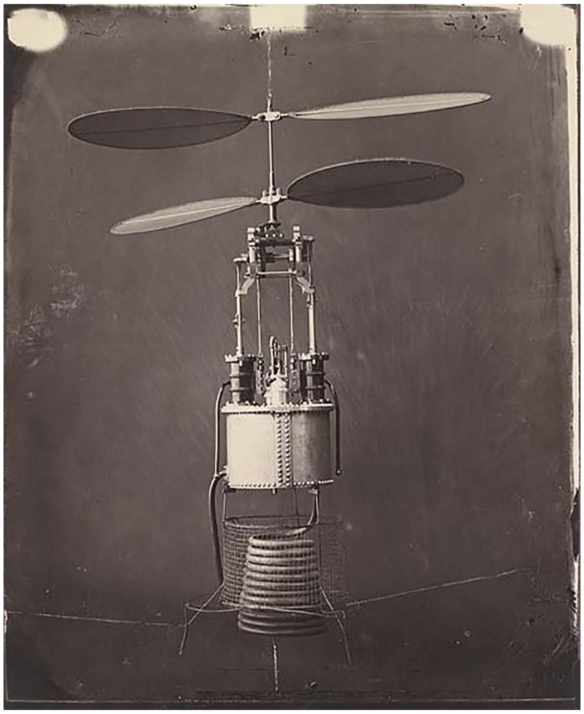

Fig. 1. d'Amécourt's hélicoptère (Nadar, Public domain, via Wikimedia Commons).

the helicopter that would fly on Mars would also be a two-bladed coaxial device (Fig. 2). d'Amécourt's device could not lift off the ground. The Mars helicopter bit into air 1% as thin as Earth and established the first powered flight outside the living planet.

The aeroelastic loads, stability, and stresses on the Mars Helicopter *Ingenuity* rotor were predicted during its design in 2015–2016 with a special-purpose three-dimensional (3D) rotor structural dynamic analysis. The stresses and strains were found to be within material limits, and the rotor to be suitable for Martian flight. That model and the analysis were not published earlier. On the morning of April 19, 2021, at 3:34 U.S. EDT, *Ingenuity* lifted off the surface of Mars and established its first flight (Ref. 1). That flight, and the 72 flights since then (last flight was on January 18, 2024), covering 10.7 miles of Martian terrain, a total flight time of 128.9 min, at speeds up to 10 m/s, have reaffirmed the validity of that analysis. This paper documents that analysis and the insights gained from it.

The development of the Mars Helicopter has been described by the Jet Propulsion Laboratory (JPL) and AeroVironment in Refs. 2–4. Details of its flight dynamics and controls are described in Ref. 5. Details of its rotor airfoils and aerodynamics are described in Ref. 6. The rotor structure and aeroelasticity are the subjects of this paper. At the time of this work, there was limited guidance on rotary-wing aeroelasticity on Mars. Only a few works dealt with the topic of rotary-wing flight on Mars at all (Refs. 7–10). The present work was undertaken upon the recommendation of Dr. Wayne Johnson of NASA to shed light on the aeroelastic behavior of the lightweight, ultra-thin (5% thickness to chord) composite rotors being developed by AeroVironment, with a special-purpose tool available at the time—X3D, under conditions anticipated, first, in the JPL chamber tests, and eventually, on Mars.

X3D Solver

The rotor analysis was performed using X3D, a 3D finite element based rotor aeroelastic solver developed at the U.S. Army Technology Development Directorate and, since 2016, at the University of Maryland (Ref. 11).

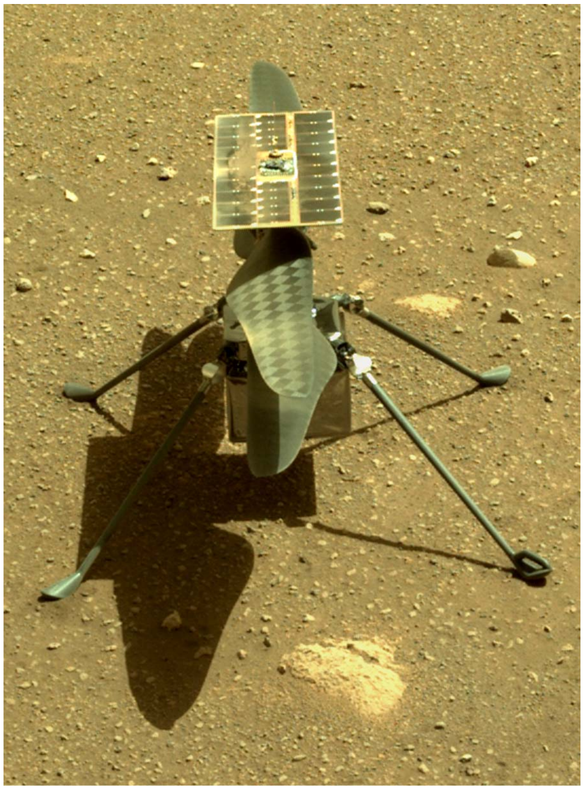

Fig. 2. Ingenuity on Mars (JPL).

X3D uses 3D nonlinear solid finite element analysis to model flexible parts of a rotor blade and multibody joints to model bearings and mechanisms. Structural deformations are solved in the rotating frame using generalized Hamilton's principle. Second Piola–Kirchhoff stresses and Green–Lagrange strains are used. The solver supports second-order 27-noded hexahedral elements. These have internal nodes that prevent shear locking for very thin elements. Each element can be assigned a 6×6 material stiffness. Only linear elastic materials are supported. The joint motions are modeled with Euler angles. The joint degrees of freedom (6) can be assigned mass, damping, and stiffness. They can also be commanded or used as load sensors. X3D includes a lifting-line aerodynamic model and an interface to couple with computational fluid dynamics (CFD). The lifting-line model is used in this work. It combines unsteady thin airfoil theory with two-dimensional (2D) airfoil tables and free wake. A built-in 1D-to-3D aerodynamic–to–structures interface redistributes lifting-line airloads on the 3D surface nodes of the finite elements.

X3D supports both transient and periodic solutions.

X3D has been expanded recently with parallel and scalable algorithms. It has been validated on single main rotor (Refs. 12, 13), tiltrotor (Refs. 14, 15), and coaxial rotor (Refs. 16, 17) configurations. It has also been used recently for the structural design of NASA and JPL's future Mars Science Helicopters (Refs. 18–21). This expanded version is used for a refined, higher resolution model.

Models

Ingenuity had a 1.21-m diameter coaxial hingeless rotor system with two independent swash-plates with collective and cyclic controls. The rotor speed was fixed.

Fig. 3. The CAD of test blade 2 from AeroVironment.

The starting point of the model was a blade Computer-Aided Design (CAD) geometry prepared by AeroVironment in the Standard for the Exchange of Product data (STEP) file format. It was a clockwise rotating blade, designated test blade 2. Figure 3 shows the CAD geometry. The rotor radius $R = 0.605$ m. The blade geometry is described in Ref. 4. The sections were based on a series of AeroVironment airfoils designed for high-altitude propellers with the camber line and thickness modified for high lift coefficient and greater spar depth. The blade had a 5% camber and 5% thickness-to-chord airfoil CLF5605 outboard of $0.527R$ with increasing thickness ratios of 5.9%, 9.8%, 22%, and 96.2% at $0.390R$, $0.295R$, $0.200R$, and $0.091R$, respectively, inboard for structural rigidity. Eight airfoil property decks covered the sectional chord Reynolds numbers (*Re*) and Mach numbers (*Ma*) encountered along the span at a rotational speed of 2,630 rpm. These were obtained by AeroVironment using the computational fluid dynamics solver Fluent. Four sets of decks were available, corresponding to various densities and speeds of sound. The decks corresponding to the lowest density $\rho = 0.012$ kg/m^3 and lowest speed of sound $a = 235$ m/s were selected for analysis. These minimized *Re* and maximized *Ma* and thus provided the severest of conditions.

Original model: ING-1

During 2015–2016, a two-bladed single rotor model was created. The blade mesh was relatively coarse for a fast solution time. Hover analysis used blade element momentum theory (BEMT) with Prandtl's tip loss. Forward flight analysis used free wake. Two turns of the wake were used. The analysis was executed on a single processor (Intel Core i7-3630QM CPU at 2.4 GHz). Each forward flight trim solution took 5–8 h of wall clock time. This model and analysis are designated the original *Ingenuity* model (ING-1) in this paper.

Refined model: ING-2

A new refined model includes both rotors. The inter-rotor spacing is $0.17R$. Both rotors use the same CAD (only flipped in orientation) so the rotors are assumed identical (Fig. 4(a)). The pitch links on the aircraft were of the same length, so the root conditions are also assumed identical. The mast is not modeled, so there is no dynamic interaction between the rotors; the only interaction is aerodynamic. The main change is the blade mesh (Fig. 4(b)). The refined mesh is an order of magnitude finer. Hover and forward flight analysis both use free wake. Six turns of the wake are used. All other properties—from blade geometry to materials to airfoil decks—remain the same. The analysis is executed in parallel on 64 processors on a single node of the University of Maryland's Zaratan cluster (AMD EPYC 7763 64-core CPUs with base clock speed of 2.45 GHz and maximum clock speed of 3.5 GHz). Each hover trim solution took around 2 h. Each forward flight trim solution took around 2 days of wall clock time. The analysis was run deliberately in the time domain (although faster periodic solution procedures were available) to ensure there were no unstable conditions. This model and analysis are designated the refined *Ingenuity* model (ING-2) in this paper.

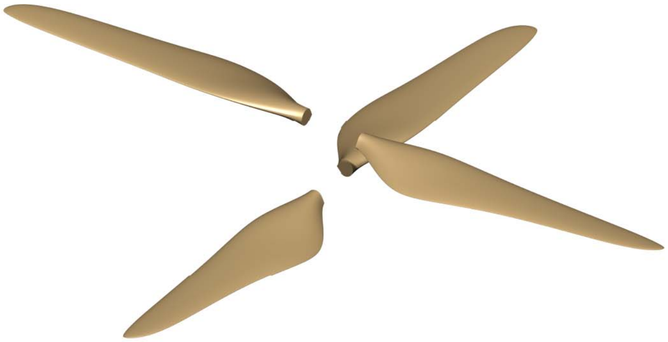

(a) The CAD model

(b) The structural mesh

Fig. 4. The structural model of the coaxial *Ingenuity* rotor.

Structural Model

The internal structure of the blade was published by AeroVironment (Refs. 3, 4). The structural model was meshed layer by layer, resolving the skin, spar caps, and the foam core, to calculate stresses and strains in all layers.

The mesh was unstructured along chord and thickness, but structured along the span so that groups of elements had coplanar faces at stations where airfoils transitioned. Later, the panels of the lifting-line aerodynamic model were made to align with these transition stations to avoid interpolating airloads before imposing on the structure. These groups were called structural segments.

A single root joint modeled the hub and the pitch bearing. It had 6 degrees of freedom—3 for translation and 3 for rotation. The rotations were modeled by Euler angles representing flap, lag, and pitch. The pitch input was commanded. Each rotor had three control angles—a collective and two cyclics. The pitch bearing stiffness was set to 250 N-m/rad. The other joint degrees of freedom were used as load sensors. In order to act as sensors, they were provided with a stiffness that was sufficiently high so as not to change the dynamics. In the absence of data, the mass and damping of the root joint were set to zero. The stiffness matrix of the root joint was diagonal, so there were no flap–lag or pitch–flap coupling at the root. One side of the joint was attached to the center of rotation, and the other side was attached to the elements that connected to the joint.

Original mesh: ING-1

The mesh used during *Ingenuity* development was coarse in the interest of time. It is designated ING-1 mesh. Its constituent parts are shown

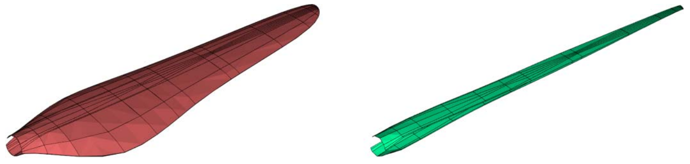

(a) Skin **(b)** Spar cap 1

(c) Spar cap 2 **(d)** Spar cap 3

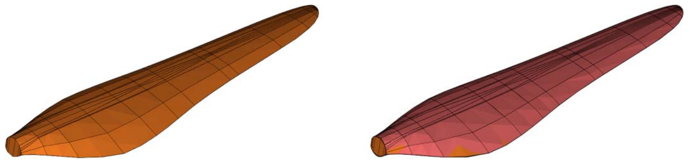

(e) Foam core **(f)** Assembled blade

Fig. 5. Original ING-1 mesh with 31,584 degrees of freedom.

in Fig. 5. At the top, there is the skin as shown in Fig. 5(a), then there is the spar, consisting of three caps as shown in Figs. 5(b)–5(d), and finally there is the foam core as shown in Fig. 5(e). Thin layers and curvatures at the trailing-edge near the root made meshing intricate. Many elements were refined manually one at a time to improve aspect ratios and eliminate negative volumes. The mesh consisted of 1,188 finite elements. The section resolution was 90. There were 13 span-wise structural segments. Each segment contained 38 surface elements, except for the last at the tip, which contained 60. These elements constituted the aerodynamic interface. The joint was attached to all 399 nodes of all 90 elements at the root end. The final structural analysis model consisted of 31,584 degrees of freedom.

Refined mesh: ING-2

The refined mesh has an order of magnitude higher resolution. This mesh is designated ING-2 mesh. Its constituent parts are shown in Fig. 6. The mesh consisted of 24,525 finite elements. The section resolution was 306. The number of span-wise structural segments was still 13 so as not to change the aerodynamic model but each segment contained many more surface elements; the first five contained 946 surface elements each, the next four contained 172, the next three contained 344, and the last segment at the tip contained 629. These elements constituted the aerodynamic interface. The joint was attached to all 1,311 nodes of all 306 elements at the root end. The final structural analysis model consisted of 630,312 degrees of freedom.

Material

Material properties were assigned for the skin, spar caps, and foam. The material densities from the manufacturer were adjusted to match measured masses and cantilevered nonrotating frequencies. These changes were justified due to unavoidable changes in properties during curing, such as resin redistribution.

There were two types of materials—foam and carbon fiber prepregs. The prepregs were bidirectional weaved cloth and unidirectional tapes.

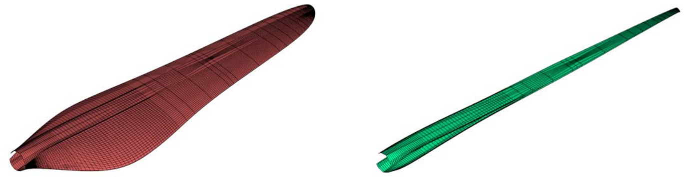

(a) Skin **(b)** Spar cap 1

(c) Spar cap 2 **(d)** Spar cap 3

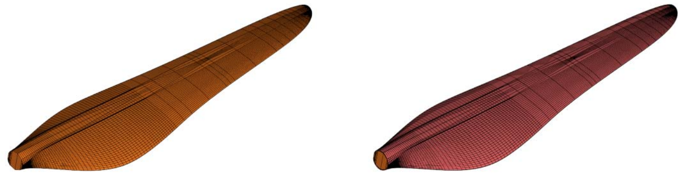

(e) Foam core **(f)** Assembled blade

Fig. 6. Refined ING-2 mesh with 630,312 degrees of freedom.

Three-dimensional modeling requires a 6×6 material stiffness matrix $\mathbf{D}$ relating stresses to strains, and the direction cosine of the material axes (say $1, 2, 3$) along which the properties are defined relative to the physical axes (say X, Y, Z) along which the deformations are defined. The stiffness matrix is generated from measured engineering constants—moduli and Poisson's ratios. The direction cosines are known from geometry.

The foam was isotropic and needed only two constants: modulus E and Poisson's ratio ν. The prepregs were orthotropic and had four constants available. These were defined in its plane (say $1-2$): moduli E_1, E_2, and G_{12} and Poisson's ratio ν_{12}. Transverse isotropy was assumed (in the $2-3$ plane) to specify the fifth constant: the Poisson's ratio, ν_{23}, which was taken equal to ν_{12}.

A complete description of an orthotropic material requires nine independent constants: E_1, E_2, E_3, ν_{12}, ν_{23}, ν_{13}, G_{12}, G_{23}, and G_{13}. Assuming transverse isotropy (in $2-3$ plane) reduces them to five: $E_1, E_2, \nu_{12}, \nu_{23}$, and G_{12}. The remaining constants are all related to these five as $E_3 = E_2$, $G_{13} = G_{12}$, $\nu_{13} = \nu_{12} = \nu$, and $2\,G_{23} = E_2/(1+\nu_{23})$. The usual relations of symmetry $\nu_{31} = (E_3/E_1)\,\nu_{13}$, $\nu_{21} = (E_2/E_1)\,\nu_{12}$, and $\nu_{32} = \nu_{23} = \nu_T$ then complete the stiffness matrix $\mathbf{D}$. These substitutions lead to $D_{22} - D_{23} = 2\,G_{23}$ in the stiffness matrix.

The allowable limits of strength (maximum stress before failure) and strain were not precisely known for the low temperatures anticipated on Mars nor the unsteady loading on the structure.

For the cloth, the limits shown in Table 1 were used for tensile, compressive, in-plane shear (IPS), and interlaminar shear (ILS). Table 2 shows the allowable strains. For the tape, the allowable stresses used are listed in Table 3. The allowable strains for the tape were the same as those for the cloth. For foam, the allowable stresses and strains are listed in Table 4. Note that these are steady limits. There is insufficient guidance for cyclic loading; for cloth and tape, the strain limits were assumed to be ± 0.0035.

Aerodynamic Model

X3D used a second-order (also called nonlinear) lifting-line (Weissinger's L) model with a 2D unsteady aerodynamic model with

Table 1. Stress limits of the cloth.

Property	Value
Tensile strength	550 MPa
Compressive strength	450 MPa
IPS	Unknown
ILS	20–45 MPa

Table 2. Strain limits of the cloth.

Load Type	Strain	Temperature
Tensile	0.0060	—
Compressive	0.0040	—
Shear	0.0180	−20 °C
	0.0100	−40 °C
	0.0080	−100 °C

Table 3. Stress limits of the tape.

Load Type	Stress (MPa)
Tensile	900
Compressive	650
IPS	90
ILS	80

Table 4. Stresses and strain limits of the foam.

Load Type	Value
Tensile	0.8 MPa
Compressive	0.4 MPa
IPS	0.4 MPa
ILS	0.4 MPa
Strain	0.009

C81 airfoil tables and free wake to calculate blade sectional airloads—lift (and bound circulation), drag, and pitching moments about quarter-chord (1/4-c). The unsteady model supplied non-circulatory airloads and a lift deficiency (Loewy) from thin airfoil theory. The lift deficiency was ignored (set to 1) in forward flight. Free wake is used to calculate the induced inflow of the rotor (Ref. 22). The inflow changes the sectional angles of attack, which in turn changes the bound circulations, so iterations are needed.

The airfoil properties are from airfoil tables (not thin airfoil properties) obtained by AeroVironment using the Fluent software and consisted of lift, drag, and 1/4-c pitching moment coefficients, c_l, c_d, and c_m, respectively, varying with angles of attack and Mach number. The effect of low Reynolds number is crucial on Mars, so tables were generated for eight Reynolds numbers from the root to the tip—for a specified air density and tip speed (or equivalently speed of sound and tip Mach number). Thus, across the blade span, eight airfoil decks are used, representing Reynolds number changes and airfoil selection. Sets of eight tables were generated for four combinations of air density and speed of sound. The combination of air density $\rho = 0.012$ kg/m^3 and speed of sound $a = 235$ m/s was selected. The viscosity used was $\mu_V = 1.15 \times 10^{-5}$ Pa s. The section Reynolds number (*Re*) is then related to the section Mach number (*Ma*) through the local chord c (in meters) by

$$\frac{Re}{Ma} = \frac{\rho\, a}{\mu_V}\ c = 247,217\ c. \tag{1}$$

The rotational speed of 2,630 rpm places the tip Mach number at 0.709. The Mach number inboard at a station r/R is then Ma $= 0.709\, r/R$. For example, a chord of $c = 0.07$ m at $r/R = 0.75$, say, would produce a Reynolds number of 9,200.

Because the Mach number (hence the Reynolds number) varies continuously over the span, the eight tables could be corrected based on the ratio of the exact Reynolds number *Re* and the table Reynolds number Re_{tab}. A similar correction would account for Reynolds number variation with azimuth in forward flight. However, this correction is not made because the advance ratio is low (0.09) and the correction is semiempirical. The Mach number variation on the advancing side was considered to be of far greater importance, which was already accounted for by the tables.

Typically, in forward flight, parameters for 2D modern unsteady aerodynamic models would be extracted from the airfoil properties. This was bypassed due to a lack of data. Of crucial importance was pitch damping, which is well captured by unsteady 2D airfoil theory. So missing from the model was dynamic stall, with no justification other than lack of data and time. The expectation was that slow flights and the absence of high-g maneuvers would prevent the onset of dynamic stall.

Tip vortex cores are expected to grow faster on Mars at a rate nominally proportional to $1/\sqrt{Re}$. The vortex core radius r_C grows with wake age ϕ (azimuth minus the azimuth when the vortex formed) as

$$\left(\frac{r_C}{c}\right)^2 = \left(\frac{r_{C0}}{c}\right)^2 + \frac{4\, a\, \delta}{(c/R)\, Re}\ \phi \tag{2}$$

where c is the chord, r_{C0} is the initial core radius, $\delta \approx 16$ for turbulent core (empirical, based on rotor test data), and $a \approx 1.25$. This means the maximum velocity induced by vortices reduces faster on Mars than on Earth, which in turn is expected to reduce vibratory loading from vortex interactions. While this is presumed to be a significant advantage on Mars, this effect was left out of the model to err on the side of higher loads. An initial core radius of $r_{C0} = 0.1c$ was used. The strength of the tip vortex was taken to be 80% of the maximum bound circulation outboard of $0.5R$. The radial location of the tip vortex release is not clear for the unusually pointed and rounded tip shape of the blade. Nevertheless, it was assumed to be at the tip ($r/R = 1.0$) to simplify the analysis. These values are typical of rotors on Earth.

Rotor Structure and Frequencies

At first, the blade mass was predicted to be 40.6 g compared to the measured mass of 35 g. Errors in skin, spar caps, and foam core were 71%, –0.5%, and –11.6%, respectively, with the highest error in the skin. It was recognized that the cured ply thickness of the skin was, in fact, lower than that of the CAD drawing by about 40%. This was accounted for by changing the skin density. That, and other small adjustments to the densities of other parts eliminated the errors. The center of gravity of the blade was predicted reasonably close to the measured value though slightly outboard span-wise, and closer to the pitch axis—upward and slightly behind. With mass distribution established, the moments of inertia about the hub could be calculated. Of these, the flapping and feathering inertia, I_b and I_f, respectively, were of particular significance to physical understanding of flap and pitch dynamics, even though they were not needed for the detailed analysis. The solidity σ was defined as the fraction of the projected blade area relative to the disk area πR^2. The projected blade area was calculated from the chord distribution at zero pitch. The mean chord $\bar{c}$ is then found from $\sigma = N_b\, \bar{c}/\pi\, R$. This chord and a mean lift curve slope of $c_{l\alpha} = 6.0$ per radian, gives a Lock number $\gamma = \rho\, c_{l\alpha}\, \bar{c}\, R^4/I_b = 0.24$. The Lock number is the ratio of aerodynamic to inertial flapping moment on the rotor. The key parameters are listed in Table 5.

Table 5. Key parameters of the blade.

Parameter	Symbol	Value	Unit
Radius	R	0.605	m
Blade mass	M_b	0.035	kg
Flap inertia	I_b	0.00285	kg-m^2
Feather inertia	I_f	1.712×10^{-5}	kg-m^2
Solidity (each rotor)	σ	0.074	
Mean chord	$\bar{c}$	0.0702	m
Lock number	γ	0.24	

Table 6. Nonrotating frequencies; measured values from AeroVironment.

Modes	Measured (Hz)	Calculated Baseline (Hz)	Calculated Refined (Hz)
Flap	64	65	64
Lag	156	142	149
Flap 2	205	219	213
Torsion	320	335	328
Flap 3	375	444	405

The nonrotating cantilevered frequencies measured by AeroVironment are given in Table 6. A 60% knockdown was needed for the skin moduli E_1 and E_2 to match the first flap frequency. With that correction, the rest of the frequencies matched reasonably well with measured values. The largest error was in torsion, predicted to be 370 Hz. However, once the blade is installed, the cantilevered condition is replaced by the control system stiffness, modeled by the pitch bearing. From nonrotating to the rotating model, the pitch bearing stiffness is an additional input. The normal practice is to measure this stiffness, but it is difficult to measure and not available a priori during a new rotor development. Thus, it was left as a parameter in the model. A stiffness of 1,000 N-m/rad effectively locked the bearing and reproduced the nonrotating cantilevered frequency of 370 Hz, whereas a stiffness of zero freed the blade in torsion and produced 0 Hz. Calculations were carried out with two values—250 and 1,000 N-m/rad. The lower stiffness was found to reduce oscillatory control loads significantly, and it also placed the torsion frequency at 335 Hz, which was much closer to the measured value. Thus, 250 N-m/rad was taken as the baseline.

The rotor frequencies varied with rotor revolutions per minute, as shown in Fig. 7 (fan plot). The refined ING-2 mesh mainly affects mode 5 (Flap 3). The small changes in modes 1–4 move predictions closer to measurements. The predicted frequencies at 2,630 rpm (43.8 Hz) are tabulated in Table 7. The rotating mode shapes are shown in Fig. 8. The modes are named after the dominant motion; however, they are coupled in general, particularly flap and torsion due to the chord-wise center of gravity offset. There are interesting patterns to be observed. Modes 3 and 5 appear to show some cross-sectional deformations—a detailed examination of which was not pursued in the interest of time. The span-wise patterns are consistent with the stresses and strains to be found later.

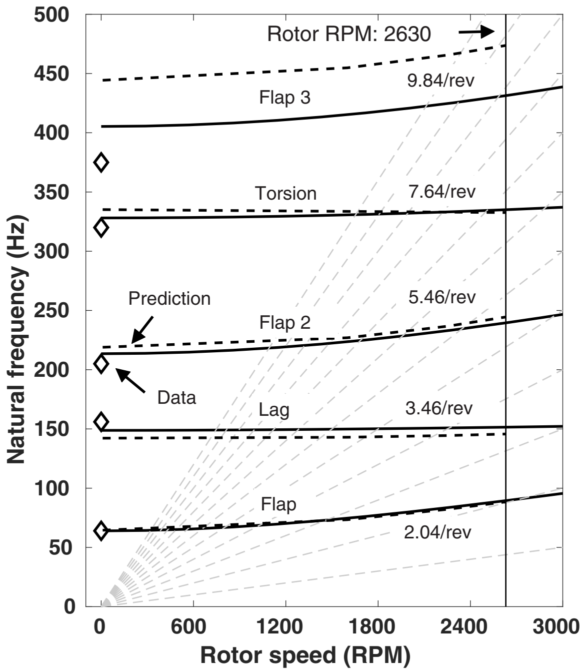

Fig. 7. Fan plot; dark dashed lines are original ING-1 model, dark solid lines are refined ING-2 model; light dashed lines are integer multiples of rotor speed in hertz; symbols are test data from AeroVironment.

Table 7. Rotating frequencies. 2630 rpm.

Modes	Baseline Mesh (Hz)	Baseline Mesh (/rev)	Refined Mesh (/rev)
Flap	89	2.03	2.04
Lag	146	3.33	3.46
Flap 2	245	5.59	5.46
Torsion	338	7.72	7.64
Flap 3	474	10.80	9.84

Hover

A collective sweep of 2°–24° was carried out to calculate maximum thrust, figure of merit (FM), blade deformations, stability, and stresses. (The collective range on the actual aircraft was −4.5° to 17.5°).

The FM versus blade loading is shown in Fig. 9. The FM is defined using the ideal induced power of a single rotor of the same (projected) disk area.

$$FM = \frac{P_{\text{ideal}}}{P} = \frac{T^{3/2}/\sqrt{2\,\rho A}}{P} \tag{3}$$

where T is the thrust in newtons, P is the power in watts, A is the projected disk area in m^2 (remains πR^2 for the coaxial), and ρ is the air density in kg/m^3.

The original ING-1 blade element momentum (BEMT) calculations predicted the maximum FM at a blade loading of around 0.17, whereas the refined ING-2 free wake calculations predict the maximum at a lower value of 0.14. Free wake is essential for proper rotor performance, but at the time the BEMT was deemed adequate to move on to focus attention on the blade stresses and strains. Test data were unavailable at the time. The measured data shown in the figure were obtained later after JPL's successful chamber tests. Two sets of data have since been published, one in Ref. 6 (Test data 1) and another in Ref. 4 (Test data 2). Predictions show similar trends. The chamber density and speed of sound were $\rho = 0.0175$ kg/m^3 and 269 m/s during the tests, which were higher than the more severe values used during design and amounted to a 40% increase in Reynolds number and a 13% decrease in Mach number. The predictions shown in Fig. 9 are at chamber conditions.

The span-wise variations of flap, lag, and axial deflections on the 1/4-c line at the highest blade loading of 0.17 are shown in Fig. 10. The

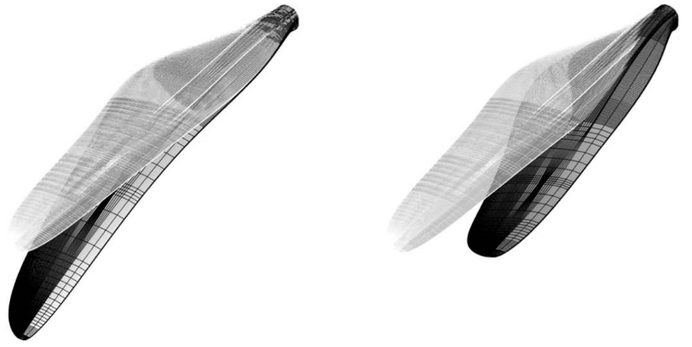

(a) Mode 1. Flap. 2.04/rev **(b)** Mode 2. Lag. 3.46/rev

(c) Mode 3. Flap 2. 5.46/rev **(d)** Mode 4. Torsion. 7.64/rev

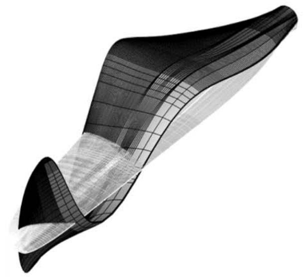

(e) Mode 5. Flap 3. 9.84/rev

Fig. 8. Mode shapes at 2630 rpm.

deformations were small; hence, they had no significant effect on hover performance. The refined ING-2 analysis showed similar deformations on both the upper and lower rotor as the first few modes were nearly identical.

The span-wise variations of airloads are shown in Fig. 11. The original ING-1 model had a single rotor, so the predictions were similar to the upper rotor hence adequate for maximum stresses. The refined ING-2 model provides a more accurate assessment of individual rotors. In the ING-2 model, the rotor is trimmed to individual torque balance and a net thrust of $C_T/\sigma = 0.14$. The lower rotor produces less thrust for the same torque naturally, as it operates in the downwash of the upper rotor (as if in a climb). The thrust share is 4.58 and 3.58 N for the upper and lower rotors, respectively—a 56% and 44% share, which is not too far away from the ideal momentum theory results of 59% and 41%. The upper rotor loading is of similar magnitude to the single rotor analysis of ING-1.

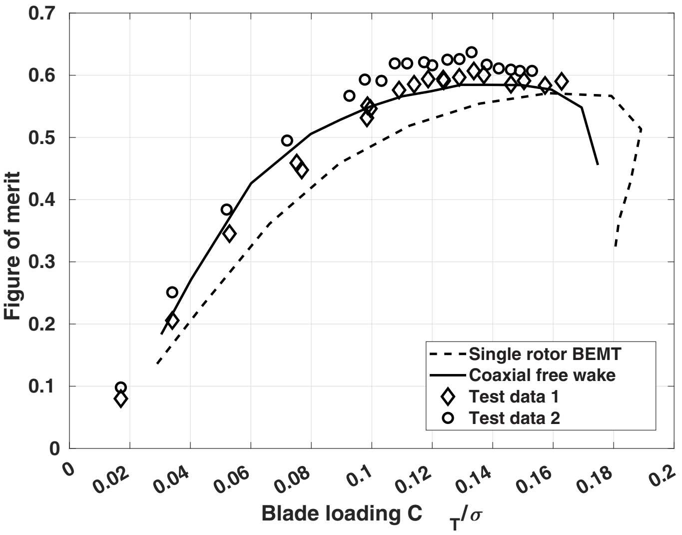

Fig. 9. Hover FM predictions versus data; predictions with single rotor BEMT and coaxial free wake models.

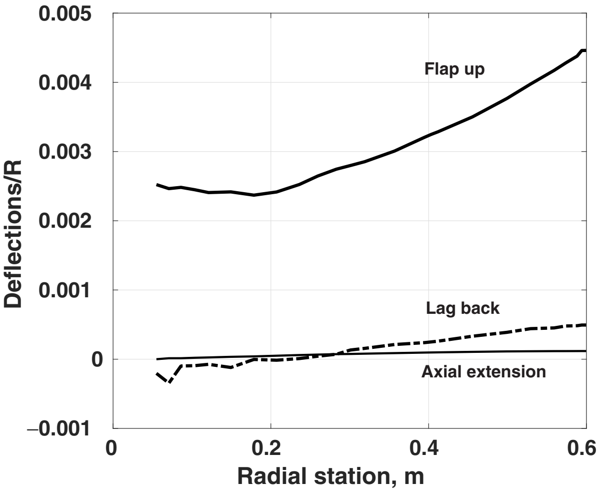

Fig. 10. Hover blade deflections versus span from single rotor BEMT analysis; $C_T/\sigma = 0.17$.

The upper rotor axial stresses and strains at $C_T/\sigma = 0.14$ are shown in Figs. 12(a) and 12(b), respectively, from the upper rotor of the ING-2 model. The loading is similar to the original ING-1 predictions, but the finer mesh of the refined ING-2 model allows a smoother variation and better resolution of the concentrations. The stresses and strains are shown in the analysis coordinates, where X is to the tip, Y to the leading-edge, and Z up in the direction of nominal thrust, not in material coordinates or natural coordinates of the elements. This gives an overall picture of the state of loading. The outer skin is removed to reveal the internal stresses. The stress levels ranged from 1 to 10 MPa on an average, but there were local concentrations up to 100 MPa inboard on the outer cap layers. The strains ranged between 100 and 200 $\mu\epsilon$ (micro-strain = strain $\times 10^6$) generally, but rising to 1000 and 2000 $\mu\epsilon$ in areas near the root. These axial stresses and strains were within limits. The shear stresses and strains were also inspected and found to be within the limits of typical prepegs—even though the exact limits at the Martian temperature were uncertain.

Of major concern was stability since rotor blades derive damping from aerodynamics, and the ultra-low density depletes it. The deflections

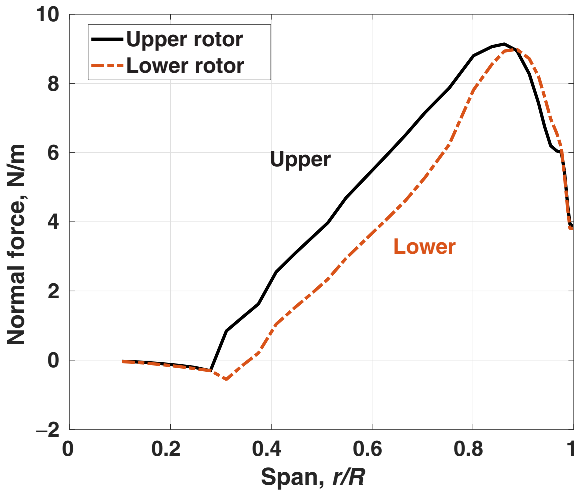

(a) Normal force, positive toward upper surface

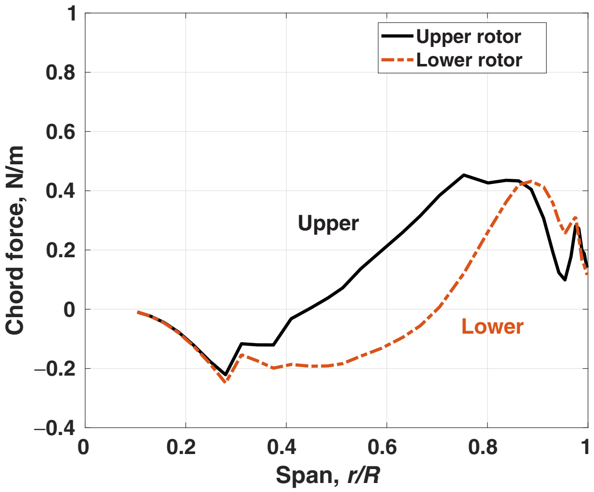

(b) Chord force, positive toward leading-edge

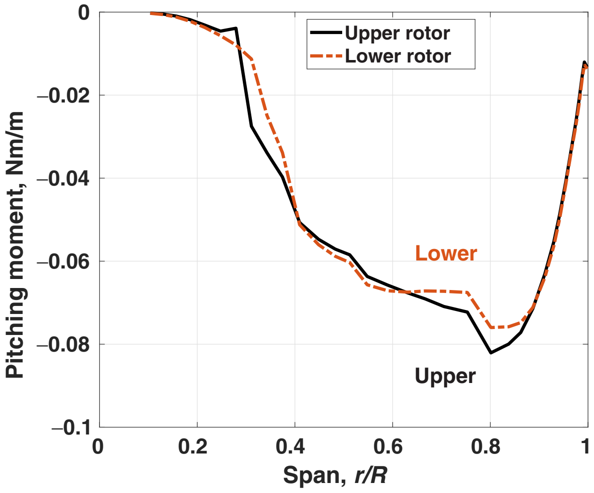

(c) 1/4-c pitching moment, positive nose up

Fig. 11. Hover airloads versus span; $C_T/\sigma = 0.12$.

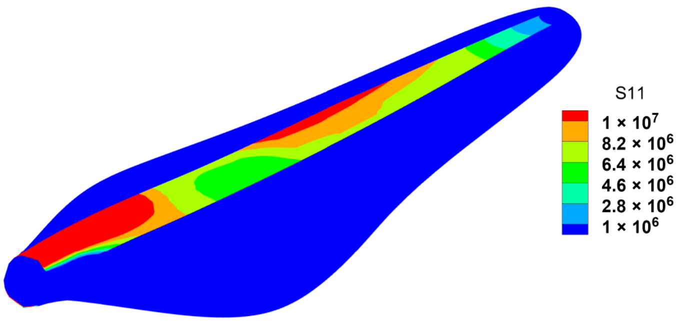

(a) S11=axial stress σ_{XX} in Pa

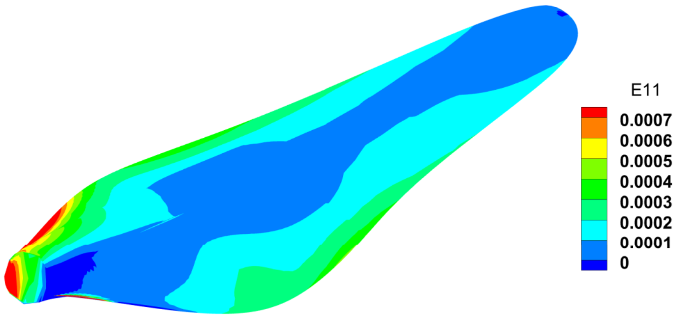

(b) E11=axial strain ϵ_{XX}

Fig. 12. Hover stresses and strains.

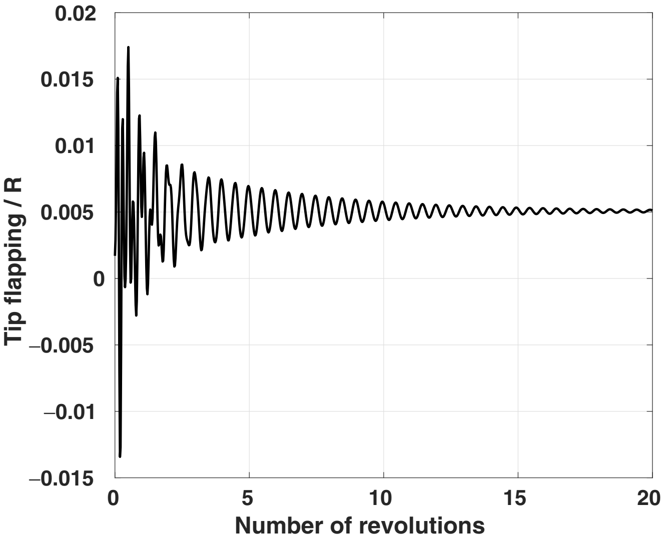

Fig. 13. Transient flapping motion at the blade tip.

shown earlier were the steady-state deflections. It took many revolutions to arrive at the steady state, often up to 20–25 revolutions depending on the condition. In order to assess stability, the hover calculations were repeated with a time marching analysis. An azimuth step of $\Delta\psi = 7.5^\circ$ (time step $\Delta t = 4.7529 \times 10^{-4}$) was used. It revealed poorly damped oscillations in flap and torsion (there was negligible motion in lag). A typical transient decay to perturbation is shown in Fig. 13. The flapping motion at the tip of the blade at 1/4-c is shown. It shows persistent flap oscillations, the effect of poor aerodynamic damping, which for the unusually stiff blades—necessary for control—meant rapid accumulation of fatigue cycles, albeit with small magnitudes. The resulting stresses/strains were also oscillatory, although lower than those encountered in forward flight.

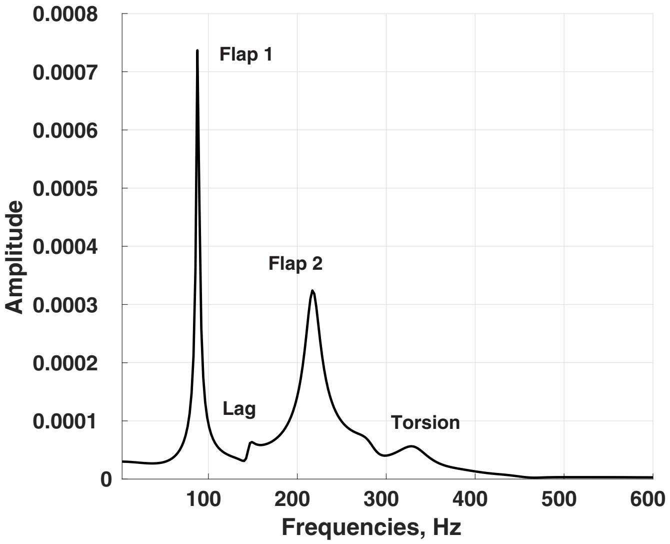

Fig. 14. Frequency response of flapping at the blade tip.

These oscillations were small in magnitude and given the very short mission times of a few minutes and a total of five missions as originally envisioned, led to a low cycle count. Therefore, fatigue loading was considered less important.

A frequency analysis of a typical perturbation decay signal of tip flapping reveals the modes (Fig. 14). Since they are coupled, there is some torsion (from center of gravity offset) and perhaps some lag (from the pitch angle at high thrust). A moving-block analysis predicted critical damping ratios of $\xi = 0.016$ (1.6%) and $\xi = 0.041$ (4.1%) in the first and second flap modes, and $\xi = 0.025$ (2.5%) in the torsion mode. Figures 15(a) and 15(b) show how the (natural logarithm of the) amplitudes vary for the flap and torsion modes as blocks of data are windowed and moved across the signal. A linear fit through this variation has the slope $-\xi\,\omega$, where ω is the frequency in radians/second. The algorithmic damping of the time-marching scheme used (generalized-α) is typically around 1%. So the actual damping is likely lower, and closer to 0.6%, 3.1%, and 1.5% in flap 1, flap 2, and torsion, respectively. The key conclusion was that even though the blade is marginally damped, the lack of modal coupling due to low Lock number made it stable, and for short flights it would hold. Note that no structural damping was added in the model, so these values are purely aeroelastic.

Forward Flight

Level flight trim solutions were examined up to a speed of 15 m/s, which was the maximum design speed of 10 m/s plus a margin of 5 m/s. Only the rotor was modeled. The shaft pitch and roll angles were specified; the roll was specified to zero.

The original ING-1 analysis modeled only a single rotor and assumed it carried half the thrust. The trim targets were rotor lift and zero hub pitch and roll moments. Trim variables were collective and longitudinal and lateral cyclic pitch angles. The shaft pitch α_S was varied from 0° to $\pm 45^\circ$. The high angles were meant to assess whether the aircraft could recover if knocked off by strong Martian winds. For the high shaft angles, the rotor was trimmed to the same lift C_L/σ (force in vertical direction) with the thrust C_T/σ (force along the shaft) increased accordingly.

The refined ING-2 analysis models the coaxial system (but still without the fuselage). The trim targets are total lift, zero net torque, and zero pitch and roll moments on individual rotors. The trim variables are three independent control angles on each rotor. Thus, there are six targets and six variables. This allowed a direct comparison to the original ING-1 analysis and generated the minimum loads and stresses that the rotor must endure.

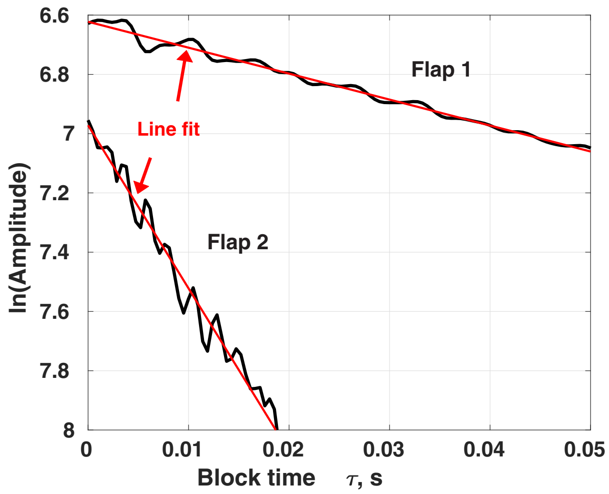

(a) Flap damping; **1.6**% and **4.1**%

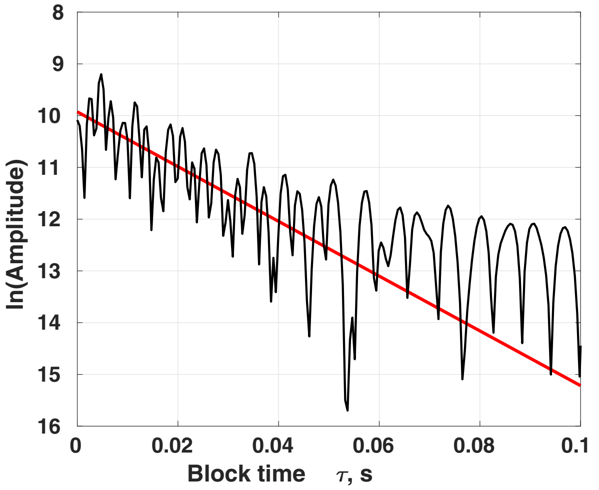

(b) Torsion damping; **2.5**%.

Fig. 15. Flap and torsion damping in hover with moving block.

In actual flight, there would likely be four trim targets—total lift, zero net torque, and net pitch and roll moments as required for vehicle equilibrium. Because counterrotating rotors naturally cancel their individual roll moments, regardless of magnitude, an additional target is the individual roll moment (normally the sum of the individual roll moments, typically divided by the thrust, to find what is called a lift offset). The five controls needed to meet these five targets are then the two collective angles on the upper and lower rotors, θ_0^U and θ_0^L, the two longitudinal cyclic angles on the upper and lower rotors θ_{1S}^U and θ_{1S}^L, and a single lateral cyclic to both rotors $\theta_{1C}^U = \theta_{1C}^L = \theta_{1C}$.

Table 8 lists the conditions analyzed. The original ING-1 analysis covered the single rotor configurations. The refined ING-2 analysis covered the coaxial. The upper rotor of the refined ING-2 analysis showed loading of similar magnitude as the original ING-1 analysis but provided a much finer resolution of stresses and strains. The refined ING-2 stress and strain results are shown here.

Table 8. Forward flight test conditions: 2630 rpm; speed of sound 235 m/s.

M_{TIP}	V (m/s)	μ	C_L/σ	α_S (deg)	Configuration
0.71					
	8.3	0.05	0.065	0°	Single
	15	0.09	0.082	0°	Single
				−45°	Single
				−30°	Single
				+30°	Single
				+45°	Single
	15	0.09	0.120	0°	Coaxial

At first, a low advance ratio, low thrust condition was explored to get a feel for Martian flight ($V = 8.3$ m/s in Table 8). The control angles were found to be low: $\theta_{75} = 6.75°$, $\theta_{1C} = 1.97°$, and $\theta_{1S} = -1.48°$. Blade loads were low. The stresses were well within limits.

Next, a higher advance ratio and thrust condition were analyzed ($V =$ 15 m/s and $C_L/\sigma = 0.082$ in Table 8). The control angles were slightly higher: $\theta_{75} = 7.28°$, $\theta_{1C} = 1.69°$, and $\theta_{1S} = -2.35°$. The blade loads were sizeable. The blade root vertical shear (lift at the root), flap moment, and lag moment were predominantly at 2/rev and determined the peak-to-peak oscillatory loading. The 2/rev resulted from the product of 1/rev velocity variation over azimuth and the 1/rev angle of attack variation due to sizeable cyclic pitch inputs. The in-plane shear (drag at the root) was predominantly at 1/rev, and it determined the oscillatory peak-to-peak loading (drag is a weaker function of angle of attack). The pitch moment (control moment, which is the pitch link load times the pitch horn) had a high steady loading, a 1/rev, and a significant 6/rev harmonic. Recall, the torsional natural frequency was between 7 and 8/rev for a pitch bearing stiffness of 250 Nm/rad. A lower stiffness of 100 Nm/rad aggravated this vibratory component significantly, whereas a higher stiffness of 1,000 Nm/rad (essentially a locked bearing) reduced it but increased the steady and 1/rev loading significantly. A stiffness of 250 Nm/rad or so seemed suitable.

The rotor could be trimmed at the high pitch angles. Short of a maneuver analysis, it indicated the rotor could generate the thrust needed and had sufficient pitch inputs to trim out over time if knocked off course by high Martian winds.

The maximum axial (bending) stresses varied from −2 MPa (compressive) to 19 MPa (tensile) over the blade. The maximum strains ranged from −200 $\mu\epsilon$ (compressive) to 400 $\mu\epsilon$ (tensile). The oscillatory stresses became significant only at higher thrust. The stresses were calculated at all azimuths (every 7.5°). For example, at azimuth $\psi = 0°$ (rear of the disk), the maximum axial (bending) stresses varied from −5 to 57 MPa and the strains from −200 to 600 $\mu\epsilon$, whereas at azimuth $\psi = 180°$ (front of the disk), the stresses varied from −6 to 65 MPa and the strains from −100 to 500 $\mu\epsilon$. These stresses and strains were well within the allowable limits. However, these are average numbers. There were significant concentrations near the root, trailing-edge, and outer layers that would benefit from a detailed examination.

Finally, the refined ING-2 model is considered in forward flight ($V =$ 15 m/s and $C_L/\sigma = 0.12$ in Table 9). The upper rotor generated 3.45 N and the lower rotor 3.35 N, which is a 51–49% thrust share. Thus, a single rotor with half the thrust was a reasonable basis for assessment. The wake geometry is shown in Fig. 16. The airloads are shown in Fig. 17. The general trends are Earth-like—the upper rotor carries a higher mean normal force (≈ lift), whereas the lower rotor carries higher oscillatory normal force. This is clear from the normal force variation versus azimuth in Fig. 17(a). The impulsive airloads in the first and fourth quadrants results from the blades passing in and out of the influence of the intertwined vortices on the advancing and retreating sides, as shown earlier in Fig. 16. The original ING-1 analysis, which was a single rotor analysis, missed this higher loading on the lower rotor, and hence underpredicted the oscillatory stresses on the lower rotor. The chord force (Fig. 17(b)) and pitching moments (Fig. 17(c)) also show the same trend in oscillatory content, although they are not as pronounced as in the normal force. Very little blade-passage impulses are observed (four times a revolution due to blades passing over each other). This is likely to be a deficiency of the lifting-line model. Contemporary work on coaxial Mars helicopters using a Reynolds-averaged Navier–Stokes solver for aerodynamics coupled with structural dynamics has revealed very high blade-passage impulsive airloads (Ref. 23).

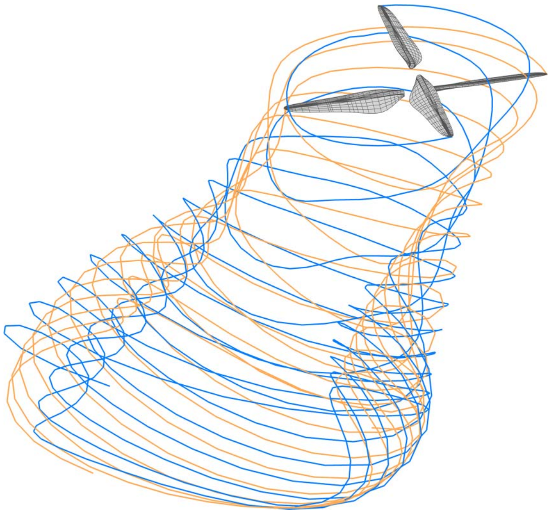

Fig. 16. Free wake trajectory in forward flight: $\mu = 0.09, C_T/\sigma = 0.12$, and $\alpha_S = 0°$.

The coaxial stresses and strains are complex, dynamic, and 3D in nature. The following series of stress and strain plots captures this complexity in a gross manner. As in hover, the stresses and strains are again shown in the analysis coordinates, where X is to the tip, Y to the leading-edge, and Z up in the direction of nominal thrust. The skin is removed to reveal the internal spar stresses and strains. These spar stresses have greater variation and variety than on the skin, although there is significant shear on the skin. The results are dynamic, but the plots show the stresses when the upper rotor is at 0° azimuth and the lower at 90°. The air speed is from the right, so the top rotor left blade is at 0° azimuth (rear) and the right blade is at 180° azimuth (front), whereas the bottom rotor left blade is at 270° azimuth (retreating from flow), and the right blade is at 90° azimuth (advancing into flow).

Figure 18 shows the axial stresses. As expected, the spar caps absorb the maximum stresses. The magnitudes are around 10 MPa with localized concentrations up to 100 MPa. All four blades appear to be in a similar state of stress, generally, because rotation still dominates the loading. The stresses are mostly tensile, although some compression is observed on the trailing edge near the root.

Figure 19 shows the normal stresses in the vertical direction. Because the skin is removed, the stresses reveal the interlaminar normal stresses (nominally, except in the regions of high curvature like the leading-edge). They are concentrated on the advancing side, from the free edge at the tip inboard, seen clearly on the lower rotor. These stresses are difficult to predict accurately, but they are also known to cause delamination.

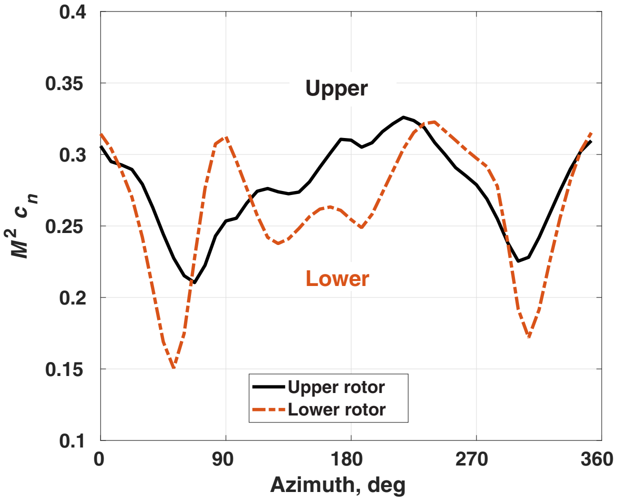

(a) Normal force coefficient, positive toward upper surface

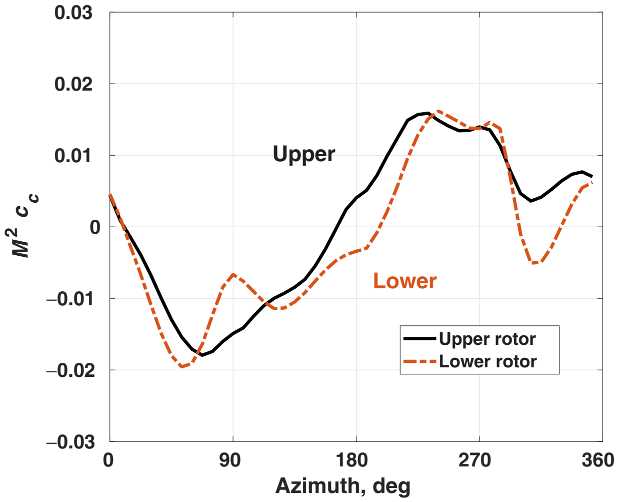

(b) Chord force coefficient, positive toward leading-edge

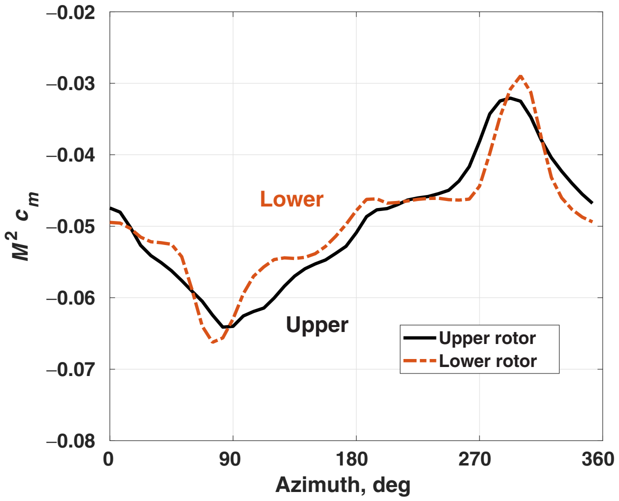

(c) 1/4-c pitching moment coefficient, positive nose up

Fig. 17. Forward flight airloads at 80%R; $\mu = 0.09$, $C_T/\sigma = 0.12$, and $\alpha_S = 0°$.

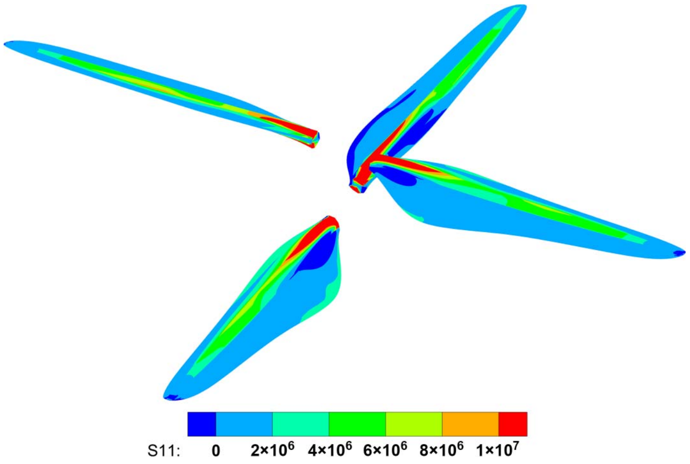

Fig. 18. Forward flight; S11 = axial stress σ_{XX} in Pa; $\mu = 0.09$ and $C_T/\sigma = 0.12$.

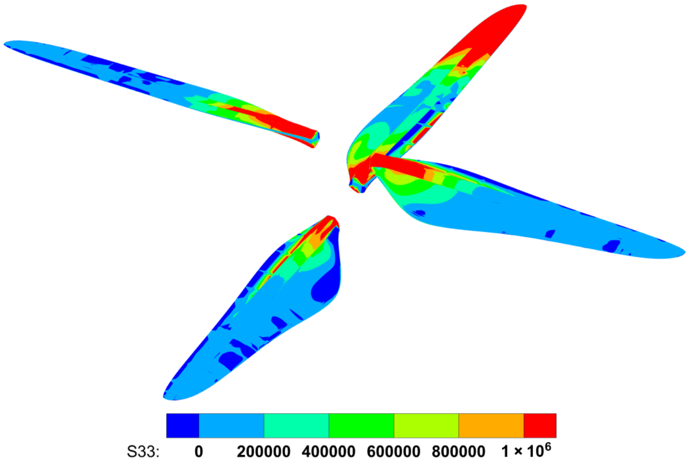

Fig. 19. Forward flight; S33 = normal stress σ_{ZZ} in Pa; $\mu = 0.09$ and $C_T/\sigma = 0.12$.

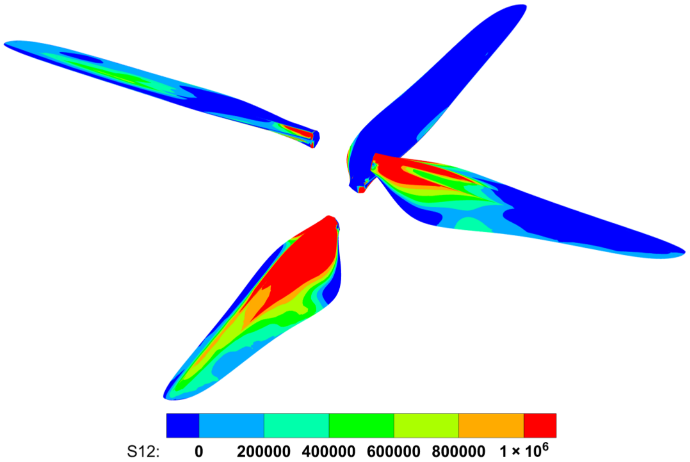

Fig. 20. Forward flight; S12 = in-plane shear stress σ_{XY} in Pa; $\mu = 0.09$ and $C_T/\sigma = 0.12$.

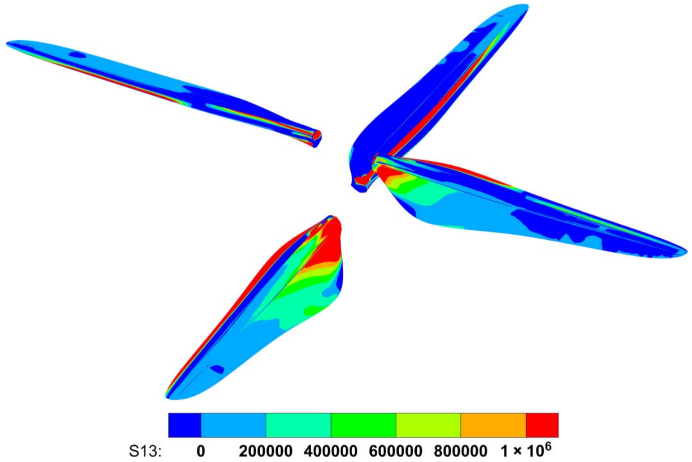

Fig. 21. Forward flight; S13 = vertical shear stress σ_{XZ} in Pa; $\mu = 0.09$ and $C_T/\sigma = 0.12$.

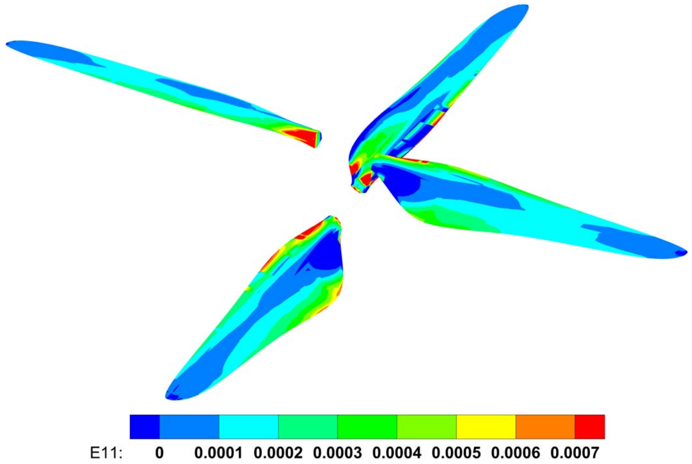

Fig. 22. Forward flight strain; E11 = axial tensile strain ϵ_{XX}; $\mu = 0.09$ and $C_T/\sigma = 0.12$.

Figure 20 shows the in-plane shear stress. Because the skin is removed, the stresses show the interlaminar shear (nominally, except in the regions of high curvature like the leading-edge). These are concentrated on the retreating side from the root end outboard, seen clearly on the lower rotor. They also appear on the front of the disk, seen clearly on the top rotor.

Figure 21 shows the vertical shear stresses. These appear generally benign, although with significant local concentrations in front of the spar caps on the advancing side, seen clearly on the lower rotor.

Figures 22 and 23 show the axial strains separately in tension and compression. Clearly, they are mainly in tension and have values up to 200–700 $\mu\epsilon$, generally with local concentrations up to twice as high. The compression is localized at the trailing edge of the curved region near the root end. The values are around 100–200 $\mu\epsilon$ generally but with higher local concentrations.

A gross assessment of axial stresses and strains averaged over a blade is tabulated in Table 9. Azimuths 0° and 180° correspond to the upper rotor. Azimuths 90° and 270° correspond to the lower rotor. Once again, there are areas of significant concentration that would benefit from a more detailed examination.

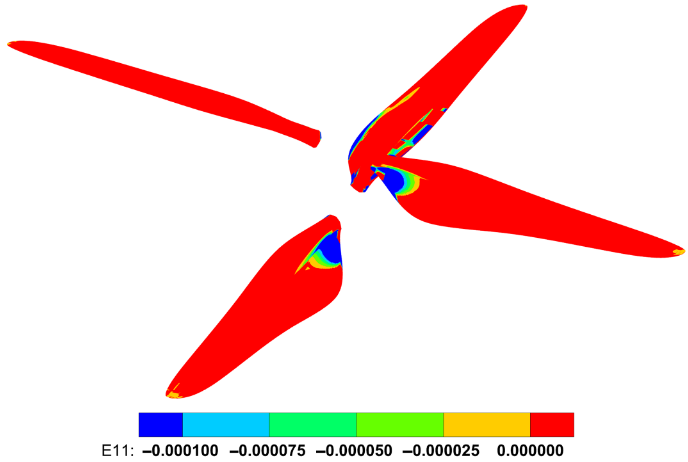

Fig. 23. Forward flight strain; E11 = axial compressive strain ϵ_{XX}; $\mu = 0.09$ and $C_T/\sigma = 0.12$.

Table 9. Maximum and minimum stresses at various azimuths: $C_T/\sigma = 0.12$, $\mu = 0.09$, and $\alpha_S = 0^\circ$.

Azimuth (deg)	Compressive Stress (MPa)	Tensile Stress (MPa)	Compression (micro-strain)	Tension (micro-strain)
0	−7.4	120	−285	700
90	−39	140	−400	750
180	None	200	−150	750
360	−28	300	−200	700

Conclusions

The Mars Helicopter rotor was modeled as a 3D structure with pitch controls coupled with a lifting-line aerodynamic model to predict aeroelastic loads, stability, and stresses in hover and controlled forward flight, under conditions anticipated on Mars. The maximum forward flight speed was 15 m/s. The unsteady lifting-line model combined 2D CFD airfoil tables and free wake. The CAD geometry and the airfoil decks were provided by AeroVironment. The analysis was performed in the U.S. Army/University of Maryland solver—X3D. The following key conclusions were drawn:

1) The rotor was structurally stable and safe to fly on Mars up to the maximum blade loading of $C_T/\sigma = 0.14$ in hover and up to a speed of 15 m/s in forward flight. But there were some caveats.

2) Aeroelastic damping is poor on Mars. The thin atmosphere depletes damping and triggers persistent flap and torsion oscillations. Compared to a typical Lock number of 8 on Earth and typical flap and torsion damping of 50% and 20%, respectively, the Lock number is only 0.24 on Mars, resulting in flap and torsion damping of only 0.5–4%. Nevertheless, the low Lock number prevents coupling between modes and keeps the rotor stable.

3) The persistent oscillations accumulate fatigue cycles quickly on Mars, more so with the unusually stiff rotor design, with the first flap frequency at or just over 2/rev.

4) Blade deformations are small on Mars because they are dominated by the centrifugal force. In hover, for example, the maximum tip flapping was calculated to be $0.0045R$ ($0.45\%R$), even at the highest blade loading. This is an order of magnitude lower than what is typical on Earth. So the oscillations, though persistent, are small.

5) The maximum blade loading predicted in hover was around $C_T/\sigma = 0.15$–0.17, depending on fidelity of aerodynamic analysis. The maximum FM was predicted around 0.58 around $C_T/\sigma = 0.14$. The blade loading is similar to Earth. The FM is low because of the high Mach low Reynolds number environment.

6) In the coaxial model, the upper rotor was predicted to carry about 56% of the total thrust in hover and about 51% in forward flight. So a single rotor analysis with half the thrust would be an adequate basis for assessment of forward flight loads.

7) In hover, the axial stresses ranged from 1 to 10 MPa on an average, but there were local concentrations upto 100 MPa. The axial strains ranged from 100 to 200 $\mu\epsilon$ (micro-strain) generally but rising to 1000–2000 $\mu\epsilon$ in some regions near the root. These stresses and strains are well within the steady limits, so the rotor is safe in hover, even at its highest blade loading.

8) In forward flight, the sectional airloads behaved similarly to that on Earth, where the upper rotor carried more steady loading, and the lower rotor carried more oscillatory loading.

9) In forward flight, the blade root shear and flap and lag moments were predominantly at 2/rev. The in-plane shear was at 1/rev. The pitch moment had a high steady loading, a 1/rev, and a significant 6/rev. A pitch bearing stiffness of 250 Nm/rad appeared suitable. A lower stiffness aggravated the vibratory loading, whereas a higher stiffness aggravated the steady and 1/rev loading.

10) In forward flight, the stress and strains were complex, dynamic, and three dimensional. At advance ratio $\mu = 0.09$ (15 m/s at 2,630 rpm) and blade loading $C_T/\sigma = 0.12$ (1.8 kg mass), the maximum axial stresses on the spar were in the range –39 to 300 MPa and interlaminar normal and shear stresses around 1 MPa. The normal stress was maximum on the advancing side, whereas the shear stress was maximum on the retreating side. The maximum axial strains on the spar were in the range of –400 (compressive) to 750 (tensile) $\mu\epsilon$. These are well within the conventional material limits, although the precise limits at Martian temperatures and for cyclic loading were not known.

In summary, the structure was capable of absorbing more loads than aerodynamics could produce. It was clear, however, given the richness of the stress/strain variations and abundance of local concentrations from where failure might initiate, a closer investigation was desired.

Several fundamental gaps remain in Martian aeromechanics. It is recommended that they be addressed for larger more capable rotorcraft. These range from unknown strength of materials under cyclic loading at low temperatures (–50 °C) to unknown rotor unsteady aerodynamics at high Mach low Reynolds number environment. Methods to insert flap damping must be explored. Prediction tools should include mast flexibility for the structure, 3D Reynolds-averaged Navier–Stokes for aerodynamics, and an exact fluid-structure interface for ultra-thin blades. The stress analysis should be extended to maneuvers. The interlaminar stresses and strains should be predicted and inspected more carefully. These remain tasks for the future.

Acknowledgments

The work of Anubhav Datta was funded by AeroVironment, Inc., under a subcontract of a Jet Propulsion Laboratory (JPL) contract, between September 1, 2015, and October 31, 2016. The work of William Staruk (graduate student at the time and presently at Joby Aviation) and later Mrinalgouda Patil (graduate student at the time and presently at Joby Aviation) was supported by the Alfred Gessow Rotorcraft Center. The work of Elizabeth Ward (graduate student at the time and presently at Bell) helped composite modeling. We thank AeroVironment Inc. and members of its Mars Helicopter team: Makato Ueno, Ben Pipenberg, Matt Keenon, and Sara Langberg for data and technical guidance, as well as its contract managers: Chris Bang, Jeanne Scott, and Gina Junge making the contract flow seamlessly. We thank JPL and members of its Mars Helicopter team: Håvard Grip, J. (Bob) Balaram, and MiMi Aung for funding this work.

References

[1] Witze, A., "Lift Off! First flight on Mars Launches New Way to Explore Worlds," *Nature News*, April 2021.

[2] Balaram, J., Canham, T., Duncan, C., Golombek, M., Grip, H. F., Johnson, W., Maki, J., Quon, A., Stern, R., and Zhu, D., "Mars Helicopter Technology Demonstrator," AIAA 2018-0023, Proceedings of the AIAA Atmospheric Flight Mechanics Conference, Kissimmee, FL, January 8–12, 2018.

[3] Pipenberg, B. T., Keennon, M. T., Tyler, J. D., Langberg, S. A., and Hibbs, B., "Design and Fabrication of the Mars Helicopter Rotor, Airframe, and Landing Gear Systems," AIAA 2019-0620, Proceedings of the SciTech Forum, San Diego, CA, January 7–11, 2019.

[4] Pipenberg, T. B., Keennon, T. W., Langberg, A. S., and Tyler, D. J., "Development of the Mars Helicopter Rotor System," Proceedings of the 75th Annual Forum of the Vertical Flight Society, Philadelphia, PA, May 13–16, 2019.

[5] Grip, H. F., Johnson, W., Malpica, C., Scharf, D. P., Mandić, M., Young, L., Allan, B., Mettler, B., Martin, M. S., and Lam, J., "Modeling and Identification of Hover Flight Dynamics for NASA's Mars Helicopter," *Journal of Guidance, Control, and Dynamics*, Vol. 43, (2), February 2020, pp. 179–194.

[6] Koning, W. J. F., Johnson, W., and Grip, H. F., "Improved Mars Helicopter Aerodynamic Rotor Model for Comprehensive Analyses," *AIAA Journal*, Vol. 57, (9), September 2019, pp. 3969–3979.

[7] Young, L., Chen, R., Aiken, E., and Briggs, G., "Design Opportunities and Challenges in the Development of Vertical Lift Planetary Aerial Vehicles," Proceedings of the American Helicopter Society Vertical Lift Aircraft Design Specialist's Meeting, San Francisco, CA, January 19–21, 2000, pp. 1–23.

[8] Datta, A., Roget, B., Griffiths, D., Pugliese, G., Sitaraman, J., Bao, J., Liu, L., and Gamard, O., "Design of a Martian Autonomous Rotary-Wing Vehicle," *Journal of Aircraft*, Vol. 40, (3), May–June 2003, pp. 461–472.

[9] Corfeld, K. J., Strawn, R. C., and Long, L. N., "Computational Aerodynamics Analysis of a Martian Rotorcraft," *Journal of the American Helicopter Society*, Vol. 49, (3), July 2004, pp. 350–356.

[10] Shrestha, R., Benedict, M., Hrishikeshavan, V., and Chopra, I., "Hover Performance of a Small-Scale Helicopter Rotor for Flying on Mars," *Journal of Aircraft*, Vol. 53, (4), July–August 2016, pp. 1160–1167.

[11] Datta, A., "X3D—A 3D Solid Finite Element Multibody Dynamic Analysis for Rotorcraft," Proceedings of the American Helicopter Society Technical Meeting on Aeromechanics Design for Vertical Lift, San Francisco, CA, January 20–22, 2016.

[12] Ward, E., Chopra, I., and Datta, A., "Rotation Frequency-Driven Extension-Torsion Coupled Self-Twisting Rotor Blades," *Journal of Aircraft*, Vol. 55, (5), September 2018, pp. 1–13.

[13] Patil, M., and Datta, A., "A Scalable Time-Parallel Solution of Periodic Rotor Dynamics in X3D," *Journal of the American Helicopter Society*, **66**, 042007 (2021).

[14] Staruk, W., Datta, A., Chopra, I., and Jayaraman, B., "An Integrated Three-Dimensional Aeromechanics Analysis of the NASA Tilt Rotor Aeroacoustic Model," *Journal of the American Helicopter Society*, **63**, 032002 (2018).

[15] Staruk, W., and Datta, A., "Gimbaled Tiltrotor Conversion Flight Loads Prediction Using Three-Dimensional Structural Analysis," *Journal of Aircraft*, Vol. 56, (2), March 2019, pp. 758–770.

[16] Patil, M., and Datta, A., "Three-Dimensional Aeromechanical Analysis of Lift Offset Coaxial Rotors: A Helios Test Case," *Journal of Aircraft*, Vol. 61, (3), May 2024, pp. 939–956.

[17] Patil, M., Lumba, R., Jayaraman, B., and Datta, A., "An Integrated Three-Dimensional Aeromechanical Analysis for the Prediction of Stresses on Modern Coaxial Rotors," *The International Journal of High Performance Computing Applications*, Vol. 38, (4), July 2024, pp. 356–376.

[18] Johnson, W., Withrow-Maser, S., Young, L., Malpica, C., Koning, W. J. F., Kuang, W., Fehler, M., Tuano, A., Chan, A., Datta, A., Chi, C., Lumba, R., Escobar, D., Balaram, J., Tzanetos, T., and Grip, H. F., "Mars Science Helicopter Conceptual Design," NASA/TM-2020-220485, March 2020, pp. 1–53.

[19] Cummings, H., Perez, B. N. P., Koning, W., Johnson, W., Young, L., Haddad, F., Romander, E., Balaram, J., Tzanetos, T., Bowman, J., Wagner, L., Withrow- Maser, S., Isaacs, E., Toney, S., Shirazi, D., Conley, S., Pipenberg, B., Datta, A., Lumba, R., Chi, C., Smith, J. K., Cornelison, C., Perez, A., Nonomura, T., and Asai, K., "Overview and Introduction of the Rotor Optimization for the Advancement of Mars eXploration (ROAMX) Project," Proceedings of the VFS Aeromechanics for Advanced Vertical Flight Technical Meeting, San Jose, CA, January 25–27, 2022.

[20] Chi, C., Lumba, R., Jung, Y. S., and Datta, A., "Aeromechanical Analysis of a Next-Generation Mars Hexacopter Rotor," *Journal of Aircraft*, Vol. 59, (6), November–December 2022, pp. 1463–1477.

[21] Lumba, R., Chi, C., Datta, A., Koning, W., Perez, P. Natalia, Cummings, H., "Structural Design and Aeromechanical Analysis of Unconventional Blades for Future Mars Rotorcraft," *Journal of the American Helicopter Society*, **68**, 042003 (2023).

[22] Shastry, A., and Datta, A., "Predicting Wake and Structural Loads in RPM Controlled Multirotor Aircraft," Proceedings of the VFS Transformative Vertical Flight Technical Meeting, San Jose, CA, January 21–23, 2020.

[23] Escobar, D., Chopra, I., and Datta, A., "High-Fidelity Aeromechanical Analysis of Coaxial Mars Helicopter," *Journal of Aircraft*, Vol. 58, (3), May 2021, pp. 609–623.